Xiangyang Wei
State Key Laboratory of Precision Measurement Technology and Instruments, Department of Precision Instrument, Tsinghua University, Beijing 100084, China
e-mail: wei-xy14@mails.tsinghua.edu.cn

Yanke Peng
State Key Laboratory of Precision Measurement Technology and Instruments, Department of Precision Instrument, Tsinghua University, Beijing 100084, China
e-mail: pengyk@mail.tsinghua.edu.cn

Gaoshan Jing
State Key Laboratory of Precision Measurement Technology and Instruments, Department of Precision Instrument, Tsinghua University, Beijing 100084, China
e-mail: jinggaoshan@ime.ac.cn

Terrence Simon
Department of Mechanical Engineering, University of Minnesota, Minneapolis, MN 55455
e-mail: simon002@umn.edu

Tianhong Cui[1]
Department of Mechanical Engineering, University of Minnesota, Minneapolis, MN 55455
e-mail: tcui@me.umn.edu

High-Performance Perovskite Solar Cells Fabricated by a Hybrid Physical–Chemical Vapor Deposition

For the first time, we used a hybrid physical–chemical vapor deposition (HPCVD) method to fabricate perovskite solar cells (PSCs) based on perovskite films with both organic cations and halogen anions. A high power conversion efficiency (PCE) of 18.1% was achieved based on a mixed perovskite film of $MA_xFA_{1-x}Pb\ (I_yBr_{1-y})_3$ and the efficiency of the PSCs with $MAPbI_3$ and $MA_xFA_{1-x}PbI_3$ films were 14.5% and 16.4%, respectively. Perovskite material components and bandgaps were precisely tuned to achieve high photoelectric conversion performance. Three different types of perovskite films employed include $MAPbI_3$, $MA_xFA_{1-x}PbI_3$, and $MA_xFA_{1-x}Pb\ (I_yBr_{1-y})_3$ (which are also designated as $MAPbI_3$, $MA_{0.89}FA_{0.11}PbI_3$, and $MA_{0.54}FA_{0.46}Pb\ (I_{0.94}Br_{0.06})_3$ with the respective bandgaps of 1.60 eV, 1.58 eV, and 1.61 eV. The experimental results demonstrate the ability to fabricate both organic cation and halogen anion mixed perovskite films by the HPCVD method and achieve easily adjustable bandgaps. In addition, the perovskite films fabricated by HPCVD have superior surface morphology, large crystal size, and low surface roughness. Eventually, this vapor-based method will have great potential in the fabrication of large-area and flexible PSCs to promote commercial application and industrialization of future PSCs. [DOI: 10.1115/1.4049326]

Keywords: perovskite solar cells, hybrid physical–chemical vapor deposition, mixed perovskite films, adjustable bandgap, energy, photovoltaics, solar

Introduction

In the last decade, solar cells based on inorganic–organic perovskite material have attracted significant research interest as a promising renewable energy technology [1]. The power conversion efficiency (PCE) of the perovskite solar cells (PSCs) has surged from 3.8% [2] to 25.2% [1] since it was first reported in 2009 [2]. The certificated PCE of PSCs has improved more than any other types of single junction solar cells, such as the CIGS (23.4%), CdTe (22.1%), and the multi-crystalline silicon solar cells (22.3%) [1]. Only the single crystal silicon solar cells (26.1%) and single crystal GaAs solar cells (27.8%) boast higher PCEs [1]. To broaden the PSCs applications in the future, it is critical to develop fabrication methods for high-performance PSCs that can be manufactured at a high deposition rate.

Compared with other commercially available inorganic solar cells, one of the excellent properties of hybrid inorganic–organic perovskite is that its components can be tuned in a larger number of ways. Superior performance can be easily achieved just by modifying organic cations or halogen anion components. A typical perovskite's formula is AMX_3, in which A represents the organic cation such as methylammonium (MA, CH_3NH_3I) and formamidinium (FA, $CH(NH_2)_2$), M represents the metal cation such as lead (Pb) and tin (Sn), and X represents the halogen anion including chlorine (Cl), bromine (Br), and iodine (I) [3]. For example, compared with the intensively investigated $MAPbI_3$, mixed perovskite films ($MA_xFA_{1-x}Pb\ (I_yBr_{1-y})_3$) can be synthesized by mixing organic cations and halogen anion components. Theoretically, the optimal bandgap of the light absorption film for solar cells is about 1.4 eV at which the highest PCE could be achieved is 33% [4]. However, the bandgap of $MAPbI_3$ is about 1.57 eV, which is much larger than the optimal bandgap of 1.4 eV. Larger bandgap can lead to narrower wavelength light absorption [5,6]. By modifying the perovskite material's components, the perovskite film's bandgap can be readily adjusted. For the $MA_xFA_{1-x}Pb\ (I_yBr_{1-y})_3$ film, a wide bandgap in the 1.48–2.23 eV range can be achieved by tuning the percentage of organic cations and halogen anions [5]. Up to now, most of the PSCs reported with PCE values larger than 20% are based on mixed perovskite layers [7–11]. Additionally, the performance of PSCs with mixed perovskite films containing the FA group show improved thermal stability and crystal phase stability with lower hysteresis [12–14]. Furthermore, surface morphology can be improved, and the defects can be reduced by introducing Br^- into the perovskite film [12,15,16]. Zhu's group shows that $MAPbI_3$ films with some Br incorporation have large crystals with micrometer size, and no pinholes [16]. By using admittance spectroscopy, Yang et al. showed that Br^- ions introduced into perovskite material to partially replace I^- ions can decrease trap state densities to improve PSCs' performance [15].

The quality of perovskite films is a critical factor in determining the efficiency of PSCs, which is greatly affected by the fabrication methods used to synthesize perovskite films [17,18]. Fabrication methods for perovskite films can be categorized into two groups: solution-based methods ("wet") [19,20] and vapor-based methods

[1]Corresponding author.

Contributed by the Solar Energy Division of ASME for publication in the JOURNAL OF SOLAR ENERGY ENGINEERING: INCLUDING WIND ENERGY AND BUILDING ENERGY CONSERVATION. Manuscript received May 7, 2020; final manuscript received November 26, 2020; published online January 12, 2021. Editor: S.A. Sherif.

("dry") [21–23]. In certain cases, solution-based methods can also be applied in a few steps or in combination with vapor-based methods to synthesize perovskite films [24,25]. Currently, the solution-based method to synthesize perovskite films has the following apparent advantages: low cost and a modest requirement for fabrication facility [17,26]. Various modified solution methods have been developed to precisely control the crystalline process and nearly all the PSCs with PCE over 20% are fabricated by these methods [27–29]. For instance, vapor or antisolvent is used in the spin coating process to increase the crystalline process while increasing evaporation of solution. Jeon et al. were first reported to use the antisolvent method to fabricate extremely uniform and dense perovskite layers [30]. By this method, the PSCs based on the above perovskite layer also obtained a high efficiency of 16.2%. By optimizing the whole spin coating process using antisolvent, Singh and Miyasaka obtained PSCs with reproducible PCEs up to 20.8% [31]. The fabrication process of the solution-based methods that can achieve high efficiency is still quite complex, as reported in the abovementioned published paper. In addition, various process parameters must be precisely controlled to promote their application in the fabrication of large-area solar cells with industrial production.

Though vapor-based methods are not as widely used as solution-based methods, several vapor-based methods have been thoroughly investigated. The first reported method used the dual source evaporation method, which was introduced by Liu et al. [21]. Two precursors, including CH_3NH_3I and $PbCl_2$, were evaporated at the same time to react into the perovskite film within dual source evaporation equipment. By this method, a higher efficiency of 15.4% was achieved. Additionally, the vapor-assistant solution process [23] and hybrid chemical vapor deposition [32] were developed for the synthesis of perovskite films. In our previously published papers, we developed a hybrid physical–chemical vapor deposition method (HPCVD) to fabricate high-quality and uniform $CH_3NH_3PbI_3$ films [33]. Meanwhile, the detailed working mechanisms were thoroughly investigated [33,34]. The fabricated $CH_3NH_3PbI_3$ films were of high quality at a fabrication temperature of only 73 °C [33]. The resulting PSCs achieved a high PCE of up to 14.7% and were highly stable. In a subsequent work, the HPCVD process parameters, such as growth temperature, vapor pressure, vapor atmosphere, and the guiding airflow in the HPCVD process were precisely controlled [18]. The fabricated PSCs based on $CH_3NH_3PbI_3$ films achieved a higher PCE up to 15.5%. Several research groups have since used vapor-based methods to fabricate mixed perovskite films. Chen et al. introduced a low-pressure, vapor-assisted solution process to fabricate $FA_xMA_{1-x}PbI_3$ based PSCs [35]. The $FA_xMA_{1-x}PbI_3$ films were obtained by mixing a series of MAI and FAI powders with different mass ratios in the CVD process. Subsequently, a high efficiency of 16.48% was achieved when the mass ratio of MAI to FAI was 4:6 [35]. Jiang et al. demonstrated a way to fabricate PSCs based on a $Cs_xFA_{1-x}PbI_3$ film. A solution-assisted vapor method and cation exchange method were combined in their work [36]. The $FAPbI_3$ films were initially fabricated by a solution-assisted vapor method and then immersed in a $CsCH_3COO$/IPA solution to get the $Cs_xFA_{1-x}PbI_3$ film. A high PCE of 15.0% was achieved by this method. Zhu et al. used a vacuum co-evaporation deposition method to deposit $PbCl_2$ and CsCl at the same time in the first step [37]. Then, the $PbCl_2$ and CsCl film were placed on a layer of MAI powder heated to 150 °C for 20 min. By this method, the fabricated PSCs obtained a high PCE of 20.13% [37]. Thus far, mixed perovskite films with halogen anions fabricated by the vapor-based method have not been reported.

In this paper, for the first time, a vapor-based method is used to fabricate mixed PSCs based on both organic cations and halogen anions. The components and bandgaps of perovskite materials fabricated by the HPCVD method are precisely adjusted to achieve high photoelectric conversion performance. The three types of fabricated perovskite material can be described as $MAPbI_3$, $MA_{0.89}FA_{0.11}PbI_3$, and $MA_{0.54}FA_{0.46}Pb(I_{0.94}Br_{0.06})_3$. The bandgap of the three kinds of perovskite material are 1.60 eV, 1.58 eV, and 1.61 eV, respectively. The PCEs of the PSCs based on the three types of perovskite films ($MA_xFA_{1-x}Pb(I_yBr_{1-y})_3$, $MA_xFA_{1-x}PbI_3$, and $MAPbI_3$) are 18.1%, 16.4%, and 14.5%, respectively. The experimental results demonstrate the feasibility of fabricating both organic cation and halogen anion mixed perovskite films by the HPCVD method. Adjustable components and bandgaps of the mixed $MA_xFA_{1-x}Pb(I_yBr_{1-y})_3$ films can be easily achieved. Ultimately, this vapor-based method has great potential for fabrication of large-area and flexible PSCs. It will help to promote the commercial application and industrialization of future PSCs.

Experimental Methods

The fabricated PSCs are composed of a planar structure of glass/FTO/TiO_2/perovskite film/Spiro-OMeTAD/Au. The cross-sectional SEM image of the perovskite solar cell based on $MAPbI_3$ film is shown in Fig. 1(*a*). A three-dimensional schematic of the perovskite solar cell device architecture is shown in Fig. 1(*b*), including the patterns of the gold electrode and etched FTO. The treatment for FTO glass and the fabrication process for TiO_2 are the same as in our previous work [18]. The difference is the fabrication process of the perovskite films. The perovskite films are $MAPbI_3$, $MA_xFA_{1-x}PbI_3$, and $MA_xFA_{1-x}Pb(I_yBr_{1-y})_3$ for different types of PSCs. Details of the fabrication process by the HPCVD

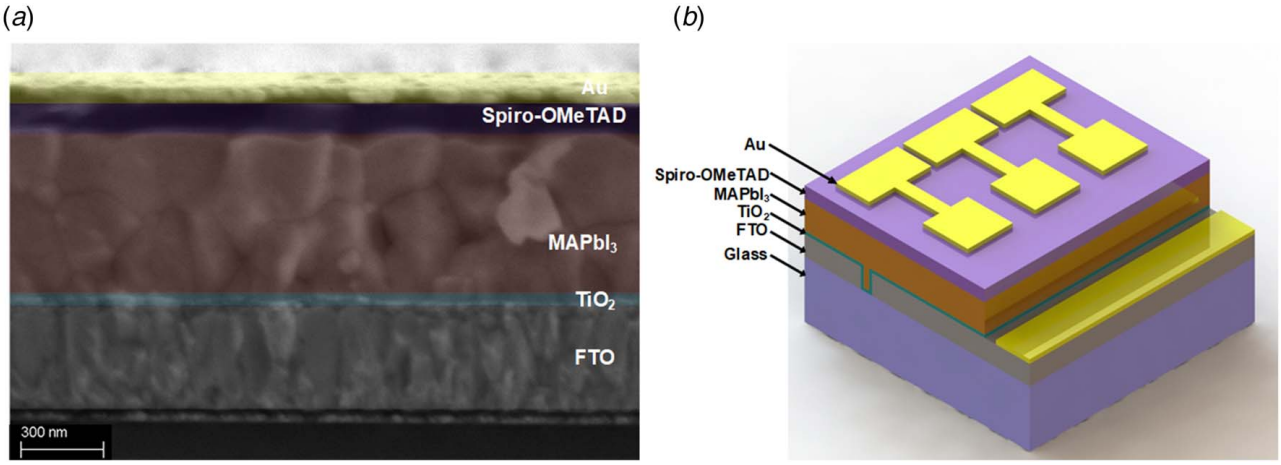

Fig. 1 (*a*) Cross-sectional SEM image and (*b*) schematic device architecture of the perovskite solar cells with a planar structure of FTO/TiO_2/$MAPbI_3$/Spiro-OMeTAD/Au

method are shown in Fig. 2. In the fabrication process of a perovskite film, a PbI_2 film was first deposited on the TiO_2/FTO/glass substrates by spin coating a 1.3 mol/l PbI_2 precursor solution. For the precursor solution, PbI_2 powder was completely dissolved into a mixed solution of N,N-dimethylformamide (DMF, Sigma) and dimethyl sulfoxide (DMSO, Sigma). The volume ratio of DMF to DMSO was 95%:5%. The spin coating process is shown in the left of Fig. 2(*a*). A speed of 2500 rpm was applied for 60 s. Next, the PbI_2 films were annealed for 60 s at a temperature of 70 °C, as shown in the right of Fig. 2(*a*). The growth process of perovskite material is different for different types of perovskite films. For the $MAPbI_3$ film shown in Fig. 2(*b*), the PbI_2 films and MAI powder were put into the CVD tube. The reaction time and growth temperature were set at 420 min and 110 °C. For the $MA_xFA_{1-x}PbI_3$ film shown in Fig. 2(*c*), the PbI_2 substrates were combined with MAI and FAI mixed powders with a mass ratio of 0.5:0.5 and were put into the CVD tube. The reaction time and growth temperature were set at 30 min and 160 °C. Lastly, for the $MA_xFA_{1-x}Pb\ (I_yBr_{1-y})_3$ film shown in Fig. 2(*d*), the PbI_2 films were combined with MABr and FAI powder with a mass ratio of 0.05: 0.95 and were put into the CVD tube. The reaction time and growth temperature were set at 420 min and 115 °C. In the CVD process, the tube was first pumped down to 20 mTorr by running a mechanical pump during the preheating process. When the temperature came to the set growth temperature, the mechanical pump was shut down to make sure that the evaporated MAI, MABr, or FAI vapor reacted with the whole PbI_2 film. Then, a Spiro-OMeTAD (Lumtech, Taiwan) film was coated on the perovskite film by spin coating at 6000 rpm as our previous work [18]. Finally, a thermal evaporation (SKY Technology Development Co. Ltd., Chinese Academy of Science, China) was used to deposit a gold layer 70 nm thick on the Spiro-OMeTAD film as the electrode. For the first 10 nm, the evaporated rate was 0.2 Å/s, and then was 0.8 Å/s for the next 60 nm. The patterns of the gold electrode were formed by using a stainless steel shadow mask in the evaporation process.

Surface morphology of perovskite films was characterized by a field-emission scanning electron microscope (FE-SEM, Zeiss Merlin, Germany). The crystalline phase and structure were characterized by X-ray diffraction (XRD) equipment. The X-ray photoelectron spectroscopy (XPS) spectrum of the three different types of perovskite films were characterized by PHI Quantera II. A UV/Vis Spectrophotometer (LAMBDA 950, PerkinElmer) was used to measure the absorption spectrum of the three types of perovskite films. An atomic force microscope (MFP-3D OriginTM, Oxford Instrument) was used to characterize the surface morphology and measure the surface roughness of the PbI_2 and perovskite films. The current density–voltage (J-V) curves were measured by a semiconductor Device Parameter Analyzer (B1500A, Keysight, Santa Rosa, CA). AM 1.5 illumination light was provided by a Newport ABB (94021A, Irvine, CA) solar simulator. A mono-silicon reference cell (Newport calibration cert, #0702, Irvine, CA) was used to calibrate the intensity of the illumination light. A stainless steel mask with an area of 9 mm^2 was used to measure the real active area of the PSCs. The voltage scanning parameters were set from −0.1 V to 1.2 V, with a step of 50 mV and a delay time of 50 ms.

Results and Discussion

In this work, we successfully fabricated two kinds of mixed perovskite films, $MA_xFA_{1-x}PbI_3$ and $MA_xFA_{1-x}Pb\ (I_yBr_{1-y})_3$, by using the HPCVD method for the first time. Simultaneously, we fabricated an $MAPbI_3$ film for comparison. For mixed perovskite films fabricated by solution-based methods, the element ratio of the film can be calculated by the ratio between different reactants [12,38]. With the vapor-based method, it is very difficult to measure the reaction rate precisely in a vacuum tube. Therefore, an accurate percentage ratio of the mixed perovskite film's components is measured by XPS, as well as XRD. The element components and distributions are shown in Fig. 3. The apparent Pb 4f, I 3d, and Br 3d characteristic peaks are used as references to analyze the ratio of different elements in the mixed perovskite films. First, Br 3d peaks, only, appear in the XPS spectrum of the $MA_xFA_{1-x}Pb\ (I_yBr_{1-y})_3$ film, as shown in Fig. 3(*c*). This demonstrates that the grown perovskite film fabricated by the HPCVD method with mixed MABr and FAI powder in the quartz tube contained Br ions. In addition, the grown perovskite films are halogen anion mixed perovskite films. Then, accurate ratios between organic cations or halogen anions were calculated by the XPS results in which a corrected relative sensitivity factor had already been applied to each element, as shown in Table 1. We can use the ratio between N and Pb to accurately calculate the ratio of MA and FA. Theoretically, each MA (CH_3NH_3) molecule contains one N atom and each FA ($CH(NH_2)_2$) contains two N atoms. As shown in Table 1, for the $MAPbI_3$ film without another organic cation, the measured ratio of N to Pb is 0.99, which is very close to the theoretical value of unity. Thus, this method is valid. Then we used this method to calculate the ratio of MA and FA cation in the $MA_xFA_{1-x}PbI_3$ and $MA_xFA_{1-x}Pb\ (I_yBr_{1-y})_3$ films. As shown in Table 1, the value of x in $MA_xFA_{1-x}PbI_3$ is 0.89 and the perovskite films can be derived as $MA_{0.89}FA_{0.11}PbI_3$. The value of x in the $MA_xFA_{1-x}Pb\ (I_yBr_{1-y})_3$ is 0.54 and the perovskite films can be derived as $MA_{0.54}FA_{0.46}Pb\ (I_yBr_{1-y})_3$. The ratio of I and Br can be directly obtained from Table 1. For the $MA_xFA_{1-x}Pb\ (I_yBr_{1-y})_3$ film, the value of y is 0.94 and $MA_xFA_{1-x}Pb\ (I_yBr_{1-y})_3$ can be derived as $MA_xFA_{1-x}Pb\ (I_{0.94}Br_{0.06})_3$. In summary, the three types of perovskite films, $MAPbI_3$, $MA_xFA_{1-x}PbI_3$, and

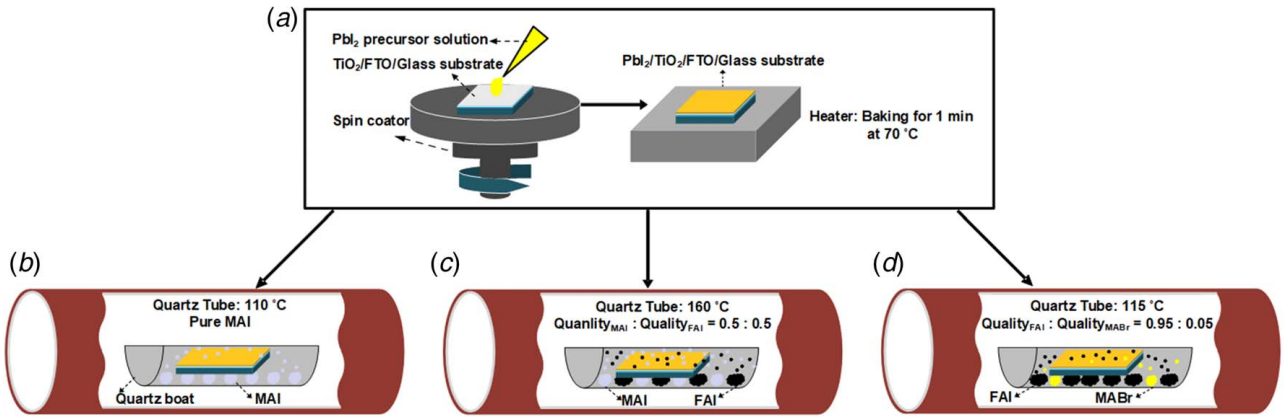

Fig. 2 Schematic diagram of the fabrication process for three different types of perovskite films ($MAPbI_3$, $MA_xFA_{1-x}PbI_3$, and $MA_xFA_{1-x}Pb\ (I_yBr_{1-y})_3$) by the HPCVD method: (*a*) fabrication of PbI_2 film, (*b*) growth of $MAPbI_3$ film by CVD method, (*c*) growth of $MA_xFA_{1-x}PbI_3$ film by CVD method, and (*d*) growth of $MA_xFA_{1-x}Pb\ (I_yBr_{1-y})_3$ film by CVD method

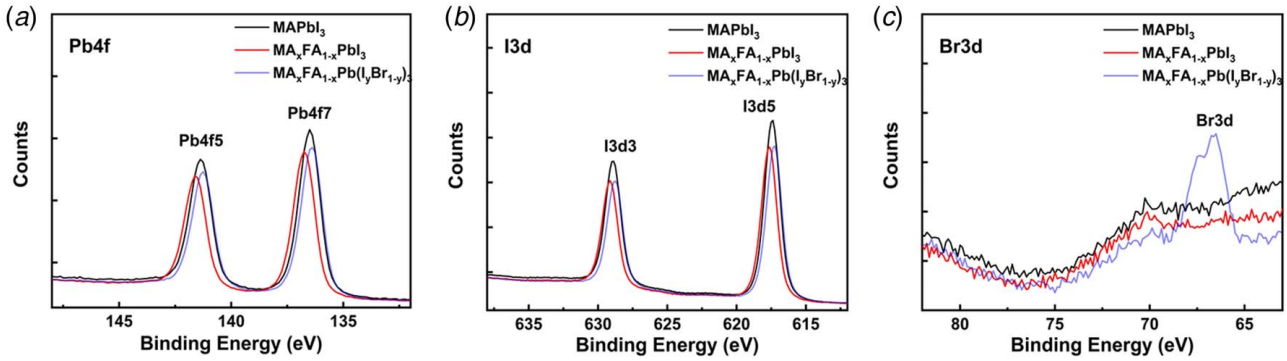

Fig. 3 XPS spectra of the three different types of perovskite films, $MAPbI_3$, $MA_xFA_{1-x}PbI_3$, and $MA_xFA_{1-x}Pb\ (I_yBr_{1-y})_3$ fabricated by the HPCVD method: (*a*) Pb 4f peak region, (*b*) I 3d peak region, and (c) Br 3d peak region

Table 1 Quantitative analysis of the atomic concentration of $MA_xFA_{1-x}Pb\ (I_yBr_{1-y})_3$ film by XPS with normalized Pb concentration

Perovskite film	N 1s	Br 3d	I 3d5	Pb 4f
$MAPbI_3$	0.99	0	2.84	1
$MA_xFA_{1-x}PbI_3$	1.11	0	2.77	1
$MA_xFA_{1-x}Pb\ (I_yBr_{1-y})_3$	1.46	0.16	2.70	1

$MA_xFA_{1-x}Pb\ (I_yBr_{1-y})_3$, can be derived as $MAPbI_3$, $MA_{0.89}FA_{0.11}PbI_3$, and $MA_{0.54}FA_{0.46}Pb\ (I_{0.94}Br_{0.06})_3$. In addition, from the XPS data for the three different kinds of perovskite films, as shown in Table 1, the ratios of Pb and anion (halogen ion) for the films are 1:2.84, 1:2.77, and 1:2.86. The three values are all close to but not exactly the theoretical value of 1:3. From the XRD results shown in Fig. 4, there is no PbI_2 residual in the three different kinds of perovskite films. We can conclude that the error regarding the ratio of Pb and halogen anions did not come from the PbI_2 residual. The reasons could be attributed to the XPS measurement process, the precision of the fitting process, decomposition of perovskite film, or possible diffusion of iodine in the perovskite material.

For the $MA_{0.54}FA_{0.46}Pb\ (I_{0.94}Br_{0.06})_3$ film, the reactants include PbI_2, FAI, and MABr. Therefore, if one MABr molecule or FAI molecule is fully involved in the reaction, the ratio of MA and Br and the ratio of FA and I, excluding the I ions coming from PbI_2, should be 1:1. However, the value we obtained from the XPS measurement regarding the ratio of MA to Br is 3:1 and the value for the ratio of FA to I, excluding the I ions coming from PbI_2, is 0.56:1. Neither were equal to the ratio in the reactants involved in the reaction. This suggests that there was a displacement reaction between different halogen ions in the CVD process. In addition, FA, MA, I, and Br ions were likely to be separately involved in the reaction, even though we used FAI and MABr as the reactants. To more precisely control the ratio between different ions in mixed $MA_xFA_{1-x}Pb\ (I_yBr_{1-y})_3$ films, more reactants, such as MAI and FABr, should be used in addition to FAI and MABr. Also, more reaction parameters, including temperature, vacuum level, and gas atmosphere should be optimized to achieve $MA_xFA_{1-x}Pb\ (I_yBr_{1-y})_3$ films with various sets of values for x and y. Further research is currently underway in our lab.

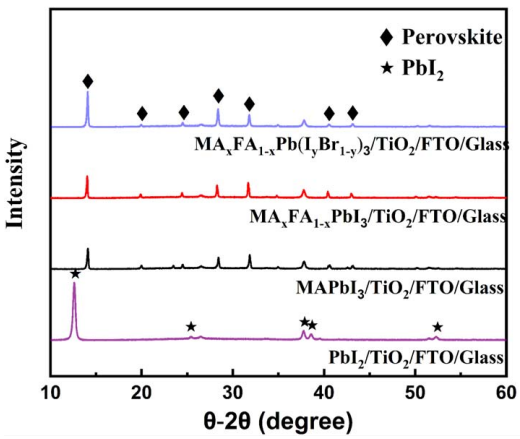

Fig. 4 XRD patterns of different types of films on TiO_2/FTO/glass, including PbI_2, $MAPbI_3$, $MA_xFA_{1-x}PbI_3$, and $MA_xFA_{1-x}Pb\ (I_yBr_{1-y})_3$

The bandgap of the mixed perovskite films fabricated by HPCVD were successfully adjusted by varying the reactant in the CVD process. The absorption spectrums of the three different types of perovskite films, including $MAPbI_3$, $MA_xFA_{1-x}PbI_3$, and $MA_xFA_{1-x}Pb\ (I_yBr_{1-y})_3$, are shown in Fig. 5(*a*). From Fig. 5, we find that the $MA_xFA_{1-x}PbI_3$ film has the highest absorbance intensity and the widest absorbance spectrum, followed by the $MAPbI_3$ film and the $MA_xFA_{1-x}Pb\ (I_yBr_{1-y})_3$ film, which has the narrowest absorbance spectrum. The bandgaps are estimated by using the absorption spectrums between 750 nm to 800 nm around the cutoff interval shown in Fig. 5(*b*). The $MA_xFA_{1-x}Pb\ (I_yBr_{1-y})_3$ film had the largest bandgap with a value about 1.61 eV, compared with 1.60 eV for the $MAPbI_3$ film and 1.58 eV for the $MA_xFA_{1-x}PbI_3$ film. The values may have some differences with the results obtained in the published results [5], but the trend is consistent with the reported results. Adjustable bandgaps of perovskite films fabricated by the HPCVD method can be achieved and the efficiency of PSCs based on the above films can be further optimized.

High performance PSCs were obtained based on the mixed perovskite films fabricated by HPCVD. The current density—voltage (J-V) curves of the highest efficiency of each of the PSCs with different types of perovskite films are shown in Fig. 6(*a*). Parameter values of these three kinds of PSCs, including PCE, short circuit current density (J_{sc}), open circuit voltage (V_{oc}), and fill factor (FF), are shown in Table 2. For the PSCs based on $MAPbI_3$, $MA_xFA_{1-x}PbI_3$ and $MA_xFA_{1-x}Pb\ (I_yBr_{1-y})_3$ films, PCE values of 14.5%, 16.4%, and 18.1% were obtained, respectively. Presented are PSCs based on each kind of perovskite film fabricated and measured. There are 14 perovskite solar cells for each of the three types. The sample-average PCE values for the three kinds of PSCs increased from 13.4% to 15.6% and 16.8%, as shown in Table 2. The efficiency distributions and performance parameters of the three kinds of PSCs are separately shown in Figs. 6(*b*) and 6(*c*).

Figure 6 shows that PSCs based on the $MA_xFA_{1-x}PbI_3$ have the highest short circuit current density (J_{sc}), about 23.3 mA/cm^2 for the champion solar cell. The reason can be attributed to its bandgap,

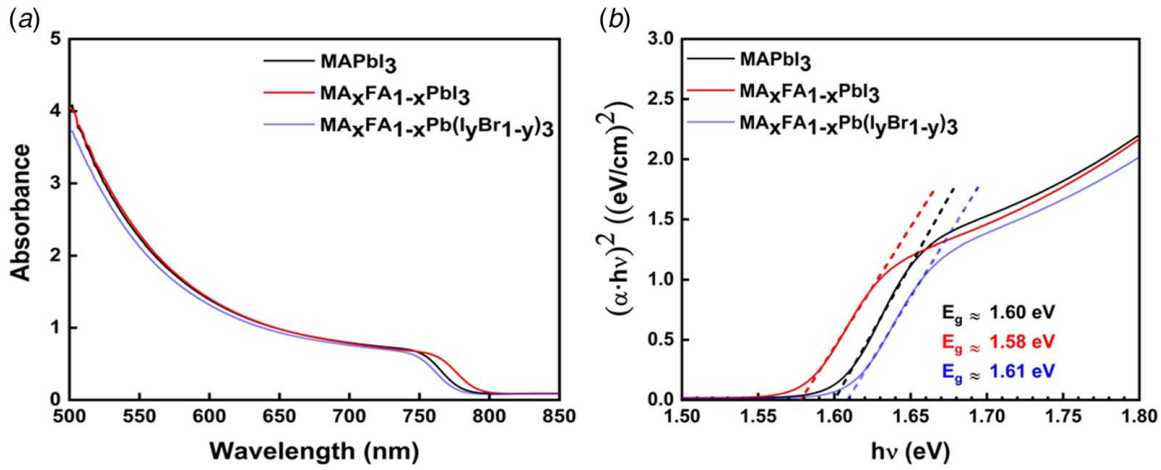

Fig. 5 (*a*) Absorbance spectrum of the three different types of perovskite films, $MAPbI_3$, $MA_xFA_{1-x}PbI_3$, and $MA_xFA_{1-x}Pb(I_yBr_{1-y})_3$, with wavelengths between 500 nm and 850 nm. (*b*) Derived bandgap of the three different types of perovskite films, $MAPbI_3$ (1.60 eV), $MA_xFA_{1-x}PbI_3$ (1.58 eV), and $MA_xFA_{1-x}Pb(I_yBr_{1-y})_3$ (1.61 eV), from the absorbance spectrum around the maximum light absorption wavelength.

which is the lowest, allowing it to absorb the widest spectrum, as noted above in Fig. 5. In addition, the top view SEM images of different types of perovskite films, $MAPbI_3$, $MA_xFA_{1-x}PbI_3$, and $MA_xFA_{1-x}Pb(I_yBr_{1-y})_3$ are shown in Fig. 7. From the SEM images, we can see that the morphology of the $MA_xFA_{1-x}PbI_3$ film is the most uniform. In addition, the $MA_xFA_{1-x}PbI_3$ films have the largest crystal size, which means that there are few grain boundary defects in the perovskite film, which is beneficial to the J_{sc}. Additionally, some reports state that $MA_xFA_{1-x}PbI_3$ films had enhanced crystallinity after FA ions incorporate into the $MAPbI_3$ crystal structure, which has a positive effect on J_{sc} [15]. Furthermore, as shown in Fig. 5(*b*), the $MA_xFA_{1-x}Pb(I_yBr_{1-y})_3$ film has a larger bandgap than the $MAPbI_3$ film, which means that the former can accommodate a narrower spectrum. However, the J_{sc} of PSCs based on $MA_xFA_{1-x}Pb(I_yBr_{1-y})_3$ film with the highest efficiency is larger than that based on $MAPbI_3$ film, 22.0 mA/cm^2 for the former and 21.3 mA/cm^2 for the latter. So were the average J_{sc} values; the former was 21.5 mA/cm^2 and the latter was for 20.8 mA/cm^2. The reason could be due to the Br ion, which can obviously decrease the defects in the perovskite films, as noted in the published results [15]. Jen's group showed that Br incorporated into a perovskite film can reduce the Pb_I antisites and help improve iodine-poor conditions. At the same time, they demonstrated that Br incorporated into the perovskite film can reduce the number of deep trap states coming from the defects or grain boundaries [15,39] in the perovskite material. In summary, compared with the other two

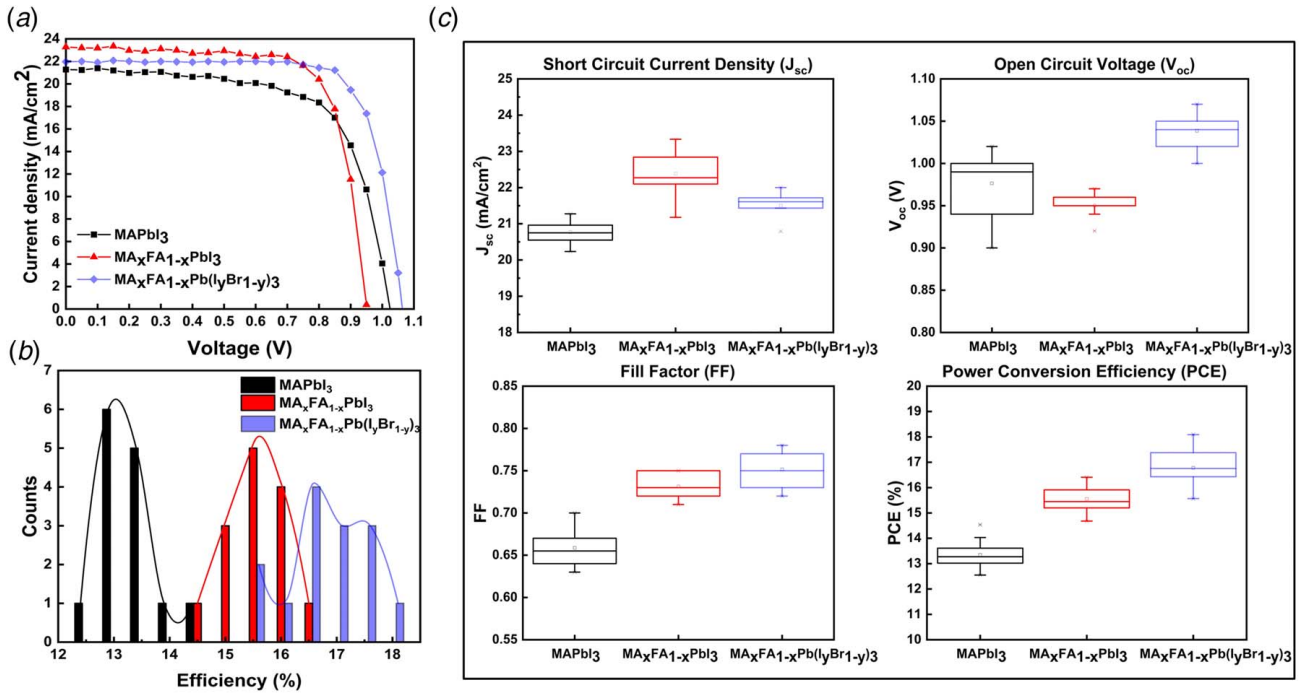

Fig. 6 (*a*) Current density–voltage (J-V) curves of the highest efficiency PSCs with different types of perovskite films, including $MAPbI_3$, $MA_xFA_{1-x}PbI_3$, and $MA_xFA_{1-x}Pb(I_yBr_{1-y})_3$. (*b*) Statistics of the efficiencies of PSCs based on the three different types of perovskite films. (*c*) Performance of the PSCs based on the three different types of perovskite films. The average PCE increased from 13.4% to 15.6% and 16.8%. Detailed information is shown in Table 2.

Table 2 Statistics of PSCs based on three different types of perovskite films including $MAPbI_3$, $MA_xFA_{1-x}PbI_3$, and $MA_xFA_{1-x}Pb(I_yBr_{1-y})_3$ fabricated by the HPCVD method

Perovskite	Types	PCE (%)	J_{sc} (mA/cm^2)	V_{oc} (V)	FF
$MAPbI_3$	Maximum	14.5	21.3	1.02	0.67
$MAPbI_3$	Mean	13.4	20.8	0.98	0.66
$MA_xFA_{1-x}PbI_3$	Maximum	16.4	23.3	0.94	0.75
$MA_xFA_{1-x}PbI_3$	Mean	15.6	22.4	0.95	0.73
$MA_xFA_{1-x}Pb(I_yBr_{1-y})_3$	Maximum	18.1	22.0	1.06	0.78
$MA_xFA_{1-x}Pb(I_yBr_{1-y})_3$	Mean	16.8	21.5	1.04	0.75

kinds of perovskite films, the $MA_xFA_{1-x}Pb(I_yBr_{1-y})_3$ film has the largest bandgap and the narrowest absorption spectrum, as shown in Fig. 5. In addition, the $MA_xFA_{1-x}Pb(I_yBr_{1-y})_3$ film has the worst surface morphology and smallest crystal size, as shown in Fig. 7. Despite this, the PSCs based on a $MA_xFA_{1-x}Pb(I_yBr_{1-y})_3$ film can still have a high J_{sc} value.

For the V_{oc}, PSCs based on a $MA_xFA_{1-x}Pb(I_yBr_{1-y})_3$ film have a high value of 1.06 V for the best performance solar cell and a value of 1.04 V for the average. The value for the PSCs based on an $MA_xFA_{1-x}PbI_3$ film is 0.94 V for the champion solar cell and 0.95 V for average. Lastly, the value for the PSCs based on an $MAPbI_3$ film is 1.02 V for the champion solar cell and 0.98 V for average. The most important reason may be the difference between energy bands for each kind of perovskite film, as shown in Fig. 5(*b*). The $MA_xFA_{1-x}Pb(I_yBr_{1-y})_3$ film has the largest V_{oc} value at 1.61 eV, compared with 1.60 eV for $MAPbI_3$ film and 1.58 eV for the $MA_xFA_{1-x}PbI_3$ film. This trend corresponds to the trend of V_{oc} in our experimental results.

Another phenomenon observed in our experimental results is that the fill factor (FF) has a huge improvement over those fabricated as mixed perovskite films with the HPCVD method. As discussed in our previous work [18], for the PSCs based on $MAPbI_3$ films fabricated by HPCVD method, we can increase the FF by increasing the spin coating speed of the PbI_2/DMF solution. However, along with the increased FF, the thickness of the perovskite film decreases, which leads to a drop in the light absorbance efficiency. However, in our study, the PSCs with the highest efficiency that are based on the $MA_xFA_{1-x}PbI_3$ and $MA_xFA_{1-x}Pb(I_yBr_{1-y})_3$ films can have a huge FF of 0.75 and 0.78, respectively, without a subsequent decrease of film thickness. The trend of average FF for three kinds of PSCs is shown in Fig. 6(*c*). Compared with the PSCs based on $MAPbI_3$ films, the FFs of the solar cells based on $MA_xFA_{1-x}PbI_3$ films show a major improvement. The reason may be the improved surface morphology and enhanced crystallization of the $MA_xFA_{1-x}PbI_3$ films, as shown in Fig. 7. For the PSCs based on a $MA_xFA_{1-x}Pb(I_yBr_{1-y})_3$ film, the FF is also further improved. Another reason may be due to Br ion inserted into the perovskite film. In addition to the reason mentioned above, Kim et al. had found that insertion of Br ions into $MAPbI_3$ can reduce the potential barrier at the apparent grain boundary [40]. This can help to enhance the FF by improving carrier collection while suppressing recombination.

Also, we conducted detailed research about PSCs based on $MA_xFA_{1-x}Pb(I_yBr_{1-y})_3$ film to identify the reasons for their excellent performance. A tapping-mode AFM height image of the PbI_2 film, the perovskite ($MA_xFA_{1-x}Pb(I_yBr_{1-y})_3$) film and the perovskite ($MAPbI_3$) film are shown in Fig. 8. Figure 8(*a*) shows that the root-mean-square (RMS) of the surface roughness of the PbI_2/TiO_2/FTO/glass substrate is only 4.4 nm, for an area of $5 \times 5\ \mu m$. Figure 8(*b*) describes the surface roughness of the $MA_xFA_{1-x}Pb(I_yBr_{1-y})_3$ /TiO_2/FTO/glass substrate fabricated by the HPCVD method. It is only 14.7 nm, for an area of $5 \times 5\ \mu m$. This is smaller than the $MAPbI_3$ film fabricated by the same process with an RMS of 17.4 nm, as shown in Fig. 8(*c*). In addition, the value of 14.7 nm is also significantly smaller than some published results [41–43]. The nonuniform surface has many negative effects on the interface characteristics. First, it would increase the carrier surface recombination at the interface between the perovskite film and the electron/hole transport layers, which would greatly decrease the performance of the device [42]. In addition, the nonuniform surface will poorly influence the spin coating process. For the PSCs fabricated in this paper, the film on the top of perovskite film was of Spiro-OMeTAD, which also was fabricated by the spin coating method. So, the nonuniform surface would result in poor quality of the Spiro-OMeTAD film. These may be the reasons why our PSCs had higher efficiency than others fabricated by a similar method. However, the perovskite solar cell with both FA^+ and Br^- mixed $MA_xFA_{1-x}Pb(I_yBr_{1-y})_3$ film had the best performance, with an efficiency of 18.1%, but with a poorer film quality, as shown in Fig. 7. We speculate that the growth rate caused by different temperatures during growth in the CVD process would be one main reason for the different surface morphologies. Another reason could be due to the different physical properties, such as boiling point and sublimation rate, of the different reactants that were used. In addition, more reactants involved in the reaction would lead to more uncontrollable variables in the growth process of the perovskite films. Furthermore, the vapor-based growth of fabricating compositional perovskite films must be optimized. A method to precisely control the ratio of different elements in the $MA_xFA_{1-x}Pb(I_yBr_{1-y})_3$ film must be found. With further improvement, we believe that a higher efficiency of PSCs based on $MA_xFA_{1-x}Pb(I_yBr_{1-y})_3$ films will be achieved.

Note that, for a planar structure perovskite solar cell with TiO_2 as the electron transport layer, hysteresis is still more pronounced than with a mesoporous structure or with inverted structure PSCs [44,45]. As mentioned before, PSCs with a planar structure have a huge hysteresis, with a PCE of 14.4% for a reverse scan and a PCE of 9.7% for a forward scan [18]. However, when we used $MA_xFA_{1-x}Pb(I_yBr_{1-y})_3$ to replace $MAPbI_3$ in the PSCs with the same structure, the hysteresis was vastly reduced. As shown in Fig. 9, PSCs based on $MA_xFA_{1-x}Pb(I_yBr_{1-y})_3$ films have better

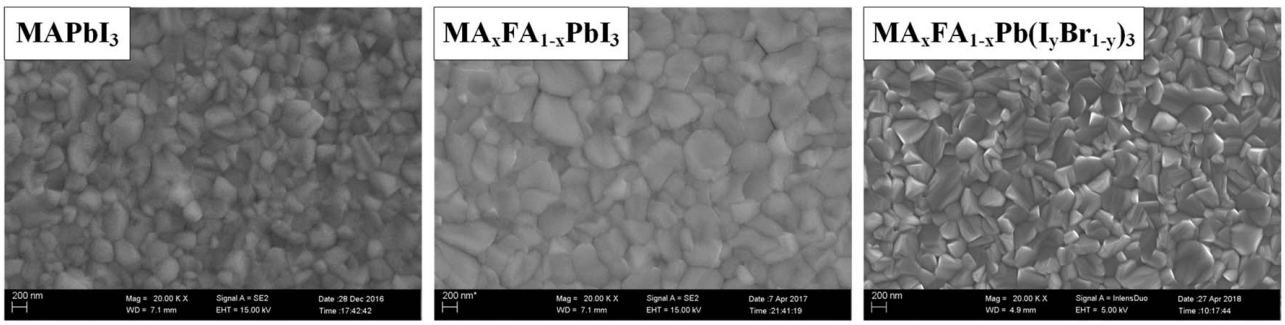

Fig. 7 Top view SEM images of different types of perovskite films, including $MAPbI_3$, $MA_xFA_{1-x}PbI_3$, and $MA_xFA_{1-x}Pb(I_yBr_{1-y})_3$, from left to right, fabricated by the HPCVD method

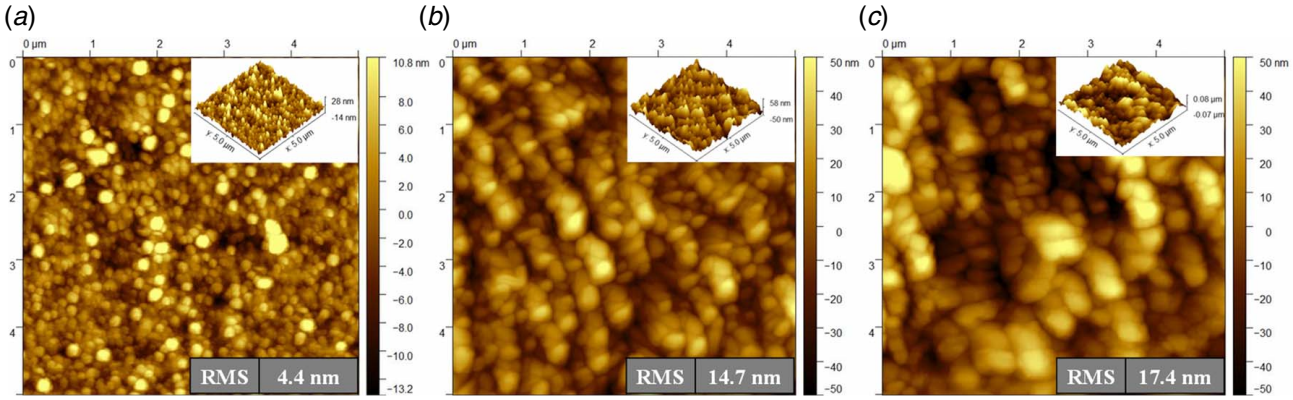

Fig. 8 Tapping-mode AFM height image of the PbI_2 film (*a*) fabricated by spin coating PbI_2/DMF + DMSO (volume ratio is 95:5) solution with surface roughness of about RMS 4.4 nm, the perovskite ($MA_xFA_{1-x}Pb$ (I_yBr_{1-y})$_3$) film, (*b*) fabricated by the HPCVD method with surface roughness of about RMS 14.7 nm, and the perovskite ($MAPbI_3$) film, and (*c*) fabricated by the HPCVD method with surface roughness of about RMS 17.4 nm, as a comparison

performance, with a reverse scan: $J_{sc} = 22.0$ mA/cm^2, $V_{oc} = 1.06$ V, FF = 0.78, and PCE = 18.1%; and a forward scan: $J_{sc} = 21.8$ mA/cm^2, $V_{oc} = 1.05$ V, FF = 0.73, and PCE = 16.6%. It is believed that ion (or defect) migration is closely related to hysteresis in PSCs, as well as the bulk or surface defects and ferroelectric properties of perovskite [44]. One reason why the hysteresis was greatly improved may be explained by the different perovskite compositions that can lead to different iodide defects and ion migration barriers. Oranskaia et al. found that PSCs based on FA-containing perovskite films have smaller hysteresis characteristics than those based on MA-containing perovskite films, because of the higher activation energy barrier of the FA-containing perovskite film [46]. Another reason why PSCs based on $MA_xFA_{1-x}Pb$ (I_yBr_{1-y})$_3$ films have smaller hysteresis characteristics can be attributed to a decrease of the bulk or surface defects in perovskite films caused by the insertion of FA and Br ions into $MAPbI_3$, as noted above [44]. However, the hysteresis in our PSCs based on $MA_xFA_{1-x}Pb$ (I_yBr_{1-y})$_3$ films still exists. Correa Baena et al. have chosen SnO_2 to replace TiO_2 as the electron transport layer in planar structured PSCs [47]. Using this method, they achieved nearly hysteresis-free PSCs with a PCE of 18.4% for a reverse scan and a PCE of 18.1% for a forward scan. Passivation layers on the upper or lower surface of perovskite film were believed to be an effective method to reduce the hysteresis in PSCs by decreasing the interface defects and surface recombination [7,48]. To be noted, an effective passivation layer must be ultrathin and very uniform, so the usual fabrication methods such as spin coating are not very proper [7,48]. Some nano-manufacturing methods [49] such as self-assembly and spray coating [50] could be used to fabricate high-quality passivation layers. We believe hysteresis in our fabricated PSCs can be further improved when different electron/hole transport layers are chosen to replace the currently used set: TiO_2 and Spiro-OMeTAD [45], or high-quality passivation layers are fabricated.

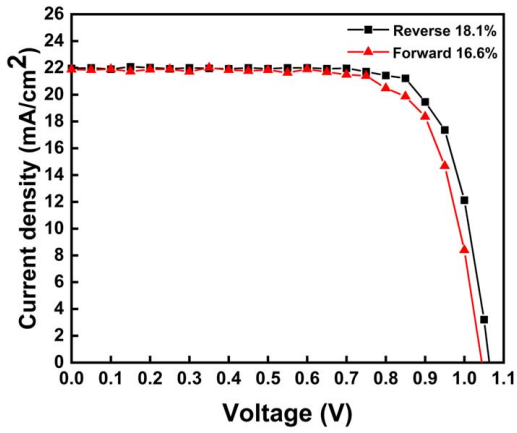

Fig. 9 Current density–voltage (J-V) curves of the champion perovskite solar cell based on an $MA_xFA_{1-x}Pb$ (I_yBr_{1-y})$_3$ film

Conclusion

In summary, a hybrid physical–chemical vapor deposition method was used to successfully fabricate perovskite films with adjustable components and bandgaps, such as $MAPbI_3$, $MA_{0.89}FA_{0.11}PbI_3$ and $MA_{0.54}FA_{0.46}Pb$ ($I_{0.94}Br_{0.06}$)$_3$. The adjustable bandgaps of these three perovskite films are 1.60 eV, 1.58 eV, and 1.61 eV, respectively. To our knowledge, this is the first time PSCs have been fabricated with halogen anion mixed perovskite films. PSCs based on $MA_{0.54}FA_{0.46}Pb$ ($I_{0.94}Br_{0.06}$)$_3$ achieved a high efficiency of 18.1%. Details regarding the vapor-based growth process research for compositional perovskite films and the methods to precisely control the ratio of different elements are discussed. We believe that PSCs with $MA_xFA_{1-x}Pb$ (I_yBr_{1-y})$_3$ will have higher efficiency and more stability in the future. In the meantime, our subsequent work will be to help develop a more competitive method to fabricate high-performance, large-area and low-cost PSCs in large-scale production to help promote commercial applications of PSCs.

Conflict of Interest

There are no conflicts of interest.

References

[1] The National Renewable Energy Laboratory (NREL), 2019, https://www.nrel.gov/pv/assets/pdfs/best-research-cell-efficiencies.20190802.pdf.
[2] Kojima, A., Teshima, K., Shirai, Y., and Miyasaka, T., 2009, "Organometal Halide Perovskites as Visible-Light Sensitizers for Photovoltaic Cells," J. Am. Chem. Soc., **131**(17), pp. 6050–6051.
[3] Xiao, J.-W., Liu, L., Zhang, D., De Marco, N., Lee, J.-W., Lin, O., Chen, Q., and Yang, Y., 2017, "The Emergence of the Mixed Perovskites and Their Applications as Solar Cells," Adv. Energy Mater., **7**(20), p. 1700491.
[4] Nelson, J., 2003, *The Physics of Solar Cells*, Imperial College Press, London.
[5] Eperon, G. E., Stranks, S. D., Menelaou, C., Johnston, M. B., Herz, L. M., and Snaith, H. J., 2014, "Formamidinium Lead Trihalide: A Broadly Tunable Perovskite for Efficient Planar Heterojunction Solar Cells," Energy Environ. Sci., **7**(3), pp. 982–988.
[6] Jung, H. S., and Park, N.-G., 2015, "Perovskite Solar Cells: From Materials to Devices," Small, **11**(1), pp. 10–25.
[7] Jiang, Q., Zhao, Y., Zhang, X., Yang, X., Chen, Y., Chu, Z., Ye, Q., Li, X., Yin, Z., and You, J., 2019, "Surface Passivation of Perovskite Film for Efficient Solar Cells," Nat. Photonics., **13**(7), pp. 460–466.

[8] Saliba, M., Correa-Baena, J.-P., Wolff, C. M., Stolterfoht, M., Phung, N., Albrecht, S., Neher, D., and Abate, A., 2018, "How to Make Over 20% Efficient Perovskite Solar Cells in Regular (n–i–p) and Inverted (p–i–n) Architectures," Chem. Mater., **30**(13), pp. 4193–4201.

[9] Jeon, N. J., Na, H., Jung, E. H., Yang, T.-Y., Lee, Y. G., Kim, G., Shin, H.-W., Il Seok, S., Lee, J., and Seo, J., 2018, "A Fluorene-Terminated Hole-Transporting Material for Highly Efficient and Stable Perovskite Solar Cells," Nat. Energy., **3**(8), pp. 682–689.

[10] Jiang, Q., Chu, Z., Wang, P., Yang, X., Liu, H., Wang, Y., Yin, Z., Wu, J., Zhang, X., and You, J., 2017, "Planar-Structure Perovskite Solar Cells with Efficiency Beyond 21," Adv. Mater., **29**(46), p. 1703852.

[11] Kim, M., Kim, G.-H., Lee, T. K., Choi, I. W., Choi, H. W., Jo, Y., Yoon, Y. J., Kim, J. W., Lee, J., Huh, D., Lee, H., Kwak, S. K., Kim, J. Y., and Kim, D. S., 2019, "Methylammonium Chloride Induces Intermediate Phase Stabilization for Efficient Perovskite Solar Cells," Joule, **3**(9), pp. 2179–2192.

[12] Salado, M., Calio, L., Berger, R., Kazim, S., and Ahmad, S., 2016, "Influence of the Mixed Organic Cation Ratio in Lead Iodide Based Perovskite on the Performance of Solar Cells," Phys. Chem. Chem. Phys., **18**(39), pp. 27148–27157.

[13] Lee, J. W., Seol, D. J., Cho, A. N., and Park, N. G., 2014, "High-Efficiency Perovskite Solar Cells Based on the Black Polymorph of $HC(NH_2)_2$ PbI_3," Adv. Mater., **26**(29), pp. 4991–4998.

[14] Pellet, N., Gao, P., Gregori, G., Yang, T. Y., Nazeeruddin, M. K., Maier, J., and Gratzel, M., 2014, "Mixed-Organic-Cation Perovskite Photovoltaics for Enhanced Solar-Light Harvesting," Angew. Chem. Int. Ed. Engl., **53**(12), pp. 3151–3157.

[15] Yang, Z., Chueh, C.-C., Liang, P.-W., Crump, M., Lin, F., Zhu, Z., and Jen, A. K. Y., 2016, "Effects of Formamidinium and Bromide Ion Substitution in Methylammonium Lead Triiodide Toward High-Performance Perovskite Solar Cells," Nano Energy, **22**, pp. 328–337.

[16] Yang, M., Zhang, T., Schulz, P., Li, Z., Li, G., Kim, D. H., Guo, N., Berry, J. J., Zhu, K., and Zhao, Y., 2016, "Facile Fabrication of Large-Grain $CH_3NH_3PbI_3$-XBrx Films for High-Efficiency Solar Cells via CH_3NH_3Br-Selective Ostwald Ripening," Nat. Commun., **7**(1), p. 12305.

[17] Green, M. A., Ho-Baillie, A., and Snaith, H. J., 2014, "The Emergence of Perovskite Solar Cells," Nat. Photonics, **8**(7), pp. 506–514.

[18] Wei, X., Peng, Y., Jing, G., and Cui, T., 2018, "Planar Structured Perovskite Solar Cells by Hybrid Physical Chemical Vapor Deposition With Optimized Perovskite Film Thickness," Jpn. J. Appl. Phys., **57**(5), p. 052301.

[19] Burschka, J., Pellet, N., Moon, S. J., Humphry-Baker, R., Gao, P., Nazeeruddin, M. K., and Gratzel, M., 2013, "Sequential Deposition as a Route to High-Performance Perovskite-Sensitized Solar Cells," Nature, **499**(7458), pp. 316–319.

[20] Im, J.-H., Jang, I.-H., Pellet, N., Grätzel, M., and Park, N.-G., 2014, "Growth of $CH_3NH_3PbI_3$ Cuboids With Controlled Size for High-Efficiency Perovskite Solar Cells," Nat. Nanotechnol., **9**(11), pp. 927–932.

[21] Liu, M., Johnston, M. B., and Snaith, H. J., 2013, "Efficient Planar Heterojunction Perovskite Solar Cells by Vapour Deposition," Nature, **501**(7467), pp. 395–398.

[22] Chen, C. W., Kang, H. W., Hsiao, S. Y., Yang, P. F., Chiang, K. M., and Lin, H. W., 2014, "Efficient and Uniform Planar-Type Perovskite Solar Cells by Simple Sequential Vacuum Deposition," Adv. Mater., **26**(38), pp. 6647–6652.

[23] Leyden, M. R., Ono, L. K., Raga, S. R., Kato, Y., Wang, S., and Qi, Y., 2014, "High Performance Perovskite Solar Cells by Hybrid Chemical Vapor Deposition," J. Mater. Chem. A., **2**(44), pp. 18742–18745.

[24] Chen, Q., Zhou, H., Song, T. B., Luo, S., Hong, Z., Duan, H. S., Dou, L., Liu, Y., and Yang, Y., 2014, "Controllable Self-Induced Passivation of Hybrid Lead Iodide Perovskites Toward High Performance Solar Cells," Nano Lett., **14**(7), pp. 4158–4163.

[25] Li, Y., Cooper, J. K., Buonsanti, R., Giannini, C., Liu, Y., Toma, F. M., and Sharp, I. D., 2015, "Fabrication of Planar Heterojunction Perovskite Solar Cells by Controlled Low-Pressure Vapor Annealing," J. Phys. Chem. Lett., **6**(3), pp. 493–499.

[26] Ono, L. K., Leyden, M. R., Wang, S., and Qi, Y., "Organometal Halide Perovskite Thin Films and Solar Cells by Vapor Deposition," J. Mater. Chem. A., **4**(18), pp. 6693–6713.

[27] Conings, B., Baeten, L., De Dobbelaere, C., D'Haen, J., Manca, J., and Boyen, H. G., 2014, "Perovskite-Based Hybrid Solar Cells Exceeding 10% Efficiency With High Reproducibility Using a Thin Film Sandwich Approach," Adv. Mater., **26**(13), pp. 2041–2046.

[28] Mitzi, D. B., Prikas, M., and Chondroudis, K., 1999, "Thin Film Deposition of Organic–Inorganic Hybrid Materials Using a Single Source Thermal Ablation Technique," Chem. Mater., **11**(3), pp. 542–544.

[29] Liang, P.-W., Liao, C.-Y., Chueh, C.-C., Zuo, F., Williams, S. T., Xin, X.-K., Lin, J., and Jen, A. K. Y., 2014, "Additive Enhanced Crystallization of Solution-Processed Perovskite for Highly Efficient Planar-Heterojunction Solar Cells," Adv. Mater., **26**(22), pp. 3748–3754.

[30] Jeon, N. J., Noh, J. H., Kim, Y. C., Yang, W. S., Ryu, S., and Seok, S. I., 2014, "Solvent Engineering for High-Performance Inorganic–Organic Hybrid Perovskite Solar Cells," Nat. Mater., **13**(9), pp. 897–903.

[31] Singh, T., and Miyasaka, T., 2017, "Stabilizing the Efficiency Beyond 20% With a Mixed Cation Perovskite Solar Cell Fabricated in Ambient Air Under Controlled Humidity," Adv. Energy Mater., **8**(3), p. 1700677.

[32] Shen, P.-S., Chen, J.-S., Chiang, Y.-H., Li, M.-H., Guo, T.-F., and Chen, P., 2016, "Low-Pressure Hybrid Chemical Vapor Growth for Efficient Perovskite Solar Cells and Large-Area Module," Adv. Mater. Interfaces, **3**(8), p. 1500849.

[33] Peng, Y., Jing, G., and Cui, T., 2015, "A Hybrid Physical–Chemical Deposition Process at Ultra-Low Temperatures for High-Performance Perovskite Solar Cells," J. Mater. Chem. A, **3**(23), pp. 12436–12442.

[34] Zhu, R., Wei, X., Xie, G., Simon, T., and Cui, T., 2020, "Numerical Simulation of Vapor Deposition Process of Perovskite Solar Cells: The Influence of Methylammonium Iodide Vapor Flow to Perovskite Growth," ASME J. Sol. Energy Eng., **143**(1), p. 011002.

[35] Chen, J., Xu, J., Xiao, L., Zhang, B., Dai, S., and Yao, J., 2017, "Mixed-Organic-Cation $(FA)_x(MA)_{1-x}PbI_3$ Planar Perovskite Solar Cells With 16.48% Efficiency via a Low-Pressure Vapor-Assisted Solution Process," ACS Appl. Mater. Interfaces, **9**(3), pp. 2449–2458.

[36] Jiang, Y., Leyden, M. R., Qiu, L., Wang, S., Ono, L. K., Wu, Z., Juarez-Perez, E. J., and Qi, Y., 2018, "Combination of Hybrid CVD and Cation Exchange for Upscaling Cs-Substituted Mixed Cation Perovskite Solar Cells With High Efficiency and Stability," Adv. Funct. Mater., **28**(1), p. 1703835.

[37] Zhu, X., Yang, D., Yang, R., Yang, B., Yang, Z., Ren, X., Zhang, J., Niu, J., Feng, J., and Liu, S., 2017, "Superior Stability for Perovskite Solar Cells With 20% Efficiency Using Vacuum Co-Evaporation," Nanoscale, **9**(34), pp. 12316–12323.

[38] Cui, P., Wei, D., Ji, J., Huang, H., Jia, E., Dou, S., Wang, T., Wang, W., and Li, M., 2019, "Planar p–n Homojunction Perovskite Solar Cells With Efficiency Exceeding 21.3%," Nat. Energy, **4**(2), pp. 150–159.

[39] Yin, W. J., Shi, T., and Yan, Y., 2014, "Unique Properties of Halide Perovskites as Possible Origins of the Superior Solar Cell Performance," Adv. Mater., **26**(27), pp. 4653–4658.

[40] Kim, G. Y., Oh, S. H., Nguyen, B. P., Jo, W., Kim, B. J., Lee, D. G., and Jung, H. S., 2015, "Efficient Carrier Separation and Intriguing Switching of Bound Charges in Inorganic-Organic Lead Halide Solar Cells," J. Phys. Chem. Lett., **6**(12), pp. 2355–2362.

[41] Chen, Q., Zhou, H., Hong, Z., Luo, S., Duan, H. S., Wang, H. H., Liu, Y., Li, G., and Yang, Y., 2014, "Planar Heterojunction Perovskite Solar Cells via Vapor-Assisted Solution Process," J. Am. Chem. Soc., **136**(2), pp. 622–625.

[42] Peng, Y., Jing, G., and Cui, T., 2015, "High-Performance Perovskite Solar Cells Fabricated by Vapor Deposition With Optimized PbI_2 precursor Films," RSC Adv., **5**(116), pp. 95847–95853.

[43] Gao, B., Meng, J., Lu, J., and Zhao, R., 2020, "$CH_3NH_3PbI_3$ Perovskite Solar Cells With Efficiency Over 22% Fabricated by Green Antisolvent Method," Mater. Lett., **274**, p. 127995.

[44] Kang, D. H., and Park, N. G., 2019, "On the Current-Voltage Hysteresis in Perovskite Solar Cells: Dependence on Perovskite Composition and Methods to Remove Hysteresis," Adv. Mater., **31**(34), p. e1805214.

[45] Chen, B., Yang, M., Priya, S., and Zhu, K., 2016, "Origin of J–V Hysteresis in Perovskite Solar Cells," J. Phys. Chem. Lett., **7**(5), pp. 905–917.

[46] Oranskaia, A., Yin, J., Bakr, O. M., Brédas, J.-L., and Mohammed, O. F., 2018, "Halogen Migration in Hybrid Perovskites: The Organic Cation Matters," J. Phys. Chem. Lett., **9**(18), pp. 5474–5480.

[47] Correa Baena, J. P., Steier, L., Tress, W., Saliba, M., Neutzner, S., Matsui, T., Giordano, F., Jacobsson, T. J., Srimath Kandada, A. R., Zakeeruddin, S. M., Petrozza, A., Abate, A., Nazeeruddin, M. K., Grätzel, M., and Hagfeldt, A., 2015, "Highly Efficient Planar Perovskite Solar Cells Through Band Alignment Engineering," Energy Environ. Sci., **8**(10), pp. 2928–2934.

[48] Wu, S., Zhang, J., Li, Z., Liu, D., Qin, M., Cheung, S. H., Lu, X., Lei, D., So, S. K., and Zhu, Z., 2020, "Modulation of Defects and Interfaces Through Alkylammonium Interlayer for Efficient Inverted Perovskite Solar Cells," Joule, **4**(6), pp. 1248–1262.

[49] Yeatman, E. M., Gramling, H. M., and Wang, E. N., 2017, "Introduction to the Special Topic on Nanomanufacturing," Microsyst. Nanoeng., **3**(1), p. 17079.

[50] Cassano, C. L., Georgiev, T. Z., and Fan, Z. H., 2017, "Using Airbrushes to Pattern Reagents for Microarrays and Paper-Fluidic Devices," Microsyst. Nanoeng., **3**(1), p. 17055.